Physics of Fluids ARTICLE scitation.org/journal/phf

Generation of streamwise helical vortex loops via successive reconnections in early pipe transition

Cite as: Phys. Fluids **34**, 054112 (2022); doi: 10.1063/5.0094326
Submitted: 2 April 2022 · Accepted: 26 April 2022 ·
Published Online: 11 May 2022

Shanxin Ruan (阮善信),[1] Shiying Xiong (熊诗颖),[1] Jiaping You (游加平),[1] and Yue Yang (杨越)[1,2,a)]

AFFILIATIONS

[1]State Key Laboratory for Turbulence and Complex Systems, College of Engineering, Peking University, Beijing 100871, China
[2]HEDPS-CAPT and BIC-ESAT, Peking University, Beijing 100871, China

[a)]Author to whom correspondence should be addressed: yyg@pku.edu.cn

ABSTRACT

We extend the vortex-surface field (VSF), a Lagrangian-based structure identification method, to investigate the vortex reconnection in temporally evolving transitional pipe flows. In the direct numerical simulation (DNS) of round pipe flows, a radial wave-like velocity disturbance is imposed on the inlet region to trigger the transition. The VSF isosurfaces are vortex surfaces composed of vortex lines, and they are concentric tubes with different wall distances at the initial time. The VSF evolution is calculated by the two-time method based on the DNS velocity field, and it is effective to identify the vortex reconnection. In the early stage of transition, the vortex surfaces are first corrugated with streamwise elongated bulges. The escalation and descent of vortex surfaces characterize the generation of high- and low-speed streaks and streamwise vortex pairs, along with the surge of the wall-friction coefficient. The resultant highly coiled and stretched vortex loops then reconnect with each other under the viscous cancelation mechanism. Subsequently, successive vortex reconnections occur via a "greedy snake" mechanism. The streamwise vortex loops consecutively capture the secondary vortex rings pinched off with self-reconnection, forming long helical vortex loops spanning over ten pipe radii in the streamwise direction. Finally, the Kelvin–Helmholtz instability of the shear layer at the trailing edge breaks down the streamwise helical vortex loops into turbulent spots.

I. INTRODUCTION

The transition to turbulence in pipe flows is one of the most fundamental and challenging problems in fluid mechanics over a century[1] and is of importance in engineering applications, such as drag reduction.[2,3] Fundamental issues in the pipe transition include the route to turbulence, the critical Reynolds number, and the mechanism of coherent structures.[4–8]

The pipe flow with a laminar profile is linearly stable, which means that, in principle, sufficiently small disturbances decay for all Reynolds numbers.[9] The subcritical feature of the pipe transition requires a disturbance with a finite magnitude to trigger the transition. The bypass transition is a common route in pipe transition studies, e.g., the blow and suction disturbance is often used to trigger the bypass transition to turbulence.[10] The formation of velocity streaks is one of the primary sources of instability in the bypass transition, and its transient growth[11–13] can lead to the secondary instability of streaks with sinuous and varicose modes. The intermittent occurrence of turbulence in pipe transitions manifests itself as puffs and slugs.[14–16] These localized structures expand, decay, and split in streamwise extent, resulting in a finite lifetime around a critical Reynolds number.[17,18] Some phenomenological models[19] have been developed to characterize a bifurcation scenario at a macroscopic level to elucidate the origin of these localized structures. However, the pipe transition is still described as "abrupt and mysterious"[18] without a detailed description of the underlying flow physics. This mystery can be partially resolved by the high-fidelity direct numerical simulation (DNS) of the spatially developing transition in long pipes.[20]

In the Lagrangian view of the transition to turbulence, the vortex reconnection[21–24] with topological changes of vortex lines, in principle, is a critical step.[25] Most existing studies of the vortex reconnection focused on relatively simple configurations of tube-like vortices, such as vortex rings,[26–28] orthogonal and antiparallel vortex tubes,[29–32] and vortex knots.[33–35] However, there appears to be no report of the vortex reconnection in the pipe transition due to its abrupt and complex nature.

In order to effectively identify the vortex reconnection in the pipe transition, we extend the vortex-surface field (VSF)[36] to pipe flows. The VSF is a Lagrangian-based method to characterize the evolution of vortex surfaces consisting of vortex lines. This method has been applied to the Klebanoff-type transitional channel flow[25] and

TABLE I. Summary and comparison of DNS parameters, where $\boldsymbol{u}_0$ denotes the initial velocity.

Case	L/R	Re	$\boldsymbol{u}_0$	m	N_x	N_r	N_θ	Δr^+	$\Delta(R\theta)^+$	Δx^+
V4	16π	5000	Eq. (3)	4	1800	256	512	0.51, 0.74	2.06	4.69
V8	16π	5000	Eq. (3)	8	1800	256	512	0.51, 0.74	2.06	4.69
V12	16π	5000	Eq. (3)	12	1800	256	512	0.51, 0.74	2.06	4.69
S8	16π	5000	Eq. (A1)	8	1800	256	512	0.51, 0.74	2.06	4.69
Ref. 39	15	5300	⋯	⋯	512	256	512	⋯	2.22	5.31
Ref. 40	30	24 580	⋯	⋯	2048	256	1024	0.8, 1.2	4.2	10.03

boundary layer.[37] The VSF evolution is able to characterize the stretching, merging, rolling-up, and twisting of vortex surfaces to elucidate the scale cascade in the transition. In particular, Zhao *et al.*[25] identified the reconnection of the hairpin-like vortical structures evolving from the initial vortex sheets in opposite halves of the channel flow using the VSF, and they found that the vortex reconnection plays a significant role in the sudden increase of the wall friction in transitional channel flows. A preliminary VSF study of the pipe transition[38] argued that the structural evolution of vortex surfaces in the transition depends on the symmetry of flow boundary conditions, so the evolution of vortex surfaces in the pipe transition can be different from those in the transitional channel and boundary-layer flows.[25,37]

In the present study, we utilize the VSF to investigate the vortex reconnection in temporally evolving transitional pipe flows. The continuous evolution of vortex surfaces from a Lagrangian perspective can shed light on the abrupt transition process in pipe flows with the characterization of vortex reconnections. The outline of this paper is as follows: in Sec. II, we describe the DNS setup and implementation of the VSF in transitional pipe flows. In Sec. III, we visualize and quantify the evolution of the vortex surfaces of the transitional pipe flow in the early stage. In particular, we reveal the formation, growth, propagation, and breakdown of streamwise helical vortex loops in the early pipe transition. Some conclusions are drawn in Sec. IV.

II. SIMULATION OVERVIEW

A. DNS of the pipe transition

We carry out the DNS of the temporally evolving transition of pipe flows by solving the three-dimensional incompressible Navier–Stokes (NS) equations

$$\frac{\partial \boldsymbol{u}}{\partial t} + \boldsymbol{u}\cdot\nabla\boldsymbol{u} = -\nabla p + \frac{1}{Re}\nabla^2\boldsymbol{u}, \tag{1}$$

$$\nabla\cdot\boldsymbol{u} = 0, \tag{2}$$

in cylindrical coordinates (x, r, θ) with the streamwise x-, radial r-, and azimuthal θ-directions, where $\boldsymbol{u} = (u_x, u_r, u_\theta)$ and p denote the non-dimensional velocity and pressure, respectively, and $Re = U_b D/\nu = 5000$ denotes the Reynolds number with the bulk streamwise velocity $U_b = 1$, the pipe diameter $D = 2$, and the kinematic viscosity $\nu = 4 \times 10^{-4}$.

The NS equations are solved in the computational domain Ω for a round pipe with the length $L = 16\pi$ and radius $R = 1$. The non-slip condition is applied at the wall, and the periodic boundary condition is used in the x-direction. The velocity $\boldsymbol{u} = (u_x, u_r, u_\theta)$ is non-dimensionalized by U_b. The number of grid points N_x, N_r, and N_θ in the three directions and other DNS parameters are listed in Table I.

In order to trigger a relatively mild transition with a clear evolution process of vortical structures, a three-dimensional, slowly time-varying wave-like disturbance fluctuating in the θ-direction with azimuthal wavenumbers $m = 4$, 8, and 12 is imposed over a time period from $t = 0$ to $t = \pi$ on the initial laminar Poiseuille flow near the left inlet boundary at $0 \le x \le 2\pi$ as

$$u_x = 2U_b\left(1 - \frac{r^2}{R^2}\right), \quad u_r = -A(t)\frac{r}{R}\cos(m\theta)\sin\left(\frac{x}{2}\right), \quad u_\theta = 0. \tag{3}$$

Here,

$$A(t) = A_0[1 - \cos(8t)]\left\{1 - \tanh\left[\frac{16}{\pi}\left(\left|t - \frac{\pi}{2}\right| - \frac{\pi}{4}\right)\right]\right\} \tag{4}$$

is the disturbance amplitude with $A_0 = 8 \times 10^{-5}$. The effects of the parameters m and A_0 on the transition process are discussed in Appendix A. In Fig. 1, the oscillation (solid line) of $A(t)$ is enveloped by a smoothed step function (dashed line) with the value $0 \le A(t) \le 4A_0$ at $0 \le t \le \pi$, mimicking a blowing and suction disturbance.[41]

This type of initial disturbance can trigger the varicose instability mode[42–47] in the early transition in cases V4, V8, and V12 in Table I. In addition, the initial disturbance in case S8 is related to the sinuous instability mode, which is discussed in Appendix A 1. Under the disturbance with the streamwise width 2π, the length of pipe 16π is long enough to reveal the structural evolution during the early transition at

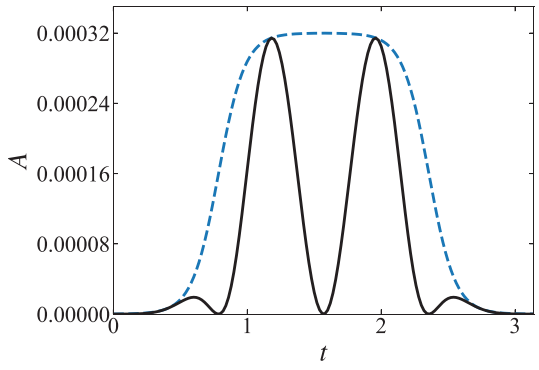

FIG. 1. Velocity disturbance amplitude (black solid line) in Eq. (4) with its envelope function (blue dashed line) in terms of time.

$0 \le t \le 15$ before the strong interaction between the leading and trailing edges of the growing disturbed region.

For the disturbance in Eq. (3), the initial components of the vorticity $\boldsymbol{\omega} = \nabla \times \boldsymbol{u}$ are

$$\omega_x = -\frac{Am}{R}\sin\left(\frac{x}{2}\right)\sin(m\theta), \quad \omega_r = 0, \\ \omega_\theta = \frac{4rU_b}{R^2} - \frac{Ar}{2R}\cos\left(\frac{x}{2}\right)\cos(m\theta), \tag{5}$$

which imply that all vortex lines lie on concentric tubes parallel to the wall. The vortex lines are integrated from Eq. (5) with $m = 8$ at $r = R$ on the x–θ surface in Fig. 2, where the artificially enlarged constant $A = A_0 \times 10^4$ is used in Eq. (4) for enhancing the visual effect of the disturbance. All the initial vortex loops are attached on the x–θ tube surface, and they induce velocities in alternating plus and minus r-directions via the Biot–Sarvart law.

In the implementation, all DNS cases are performed by the NGA code.[48] The NS equations are solved on a staggered grid in the cylindrical coordinates, and they are advanced in time by the second-order semi-implicit Crank–Nicolson scheme with the time step Δt. The pressure Poisson equation is solved to enforce continuity using a combination of spectral, Krylov-based, and multi-grid methods. The momentum equations are discretized with a second-order, centered, kinetic-energy conservative finite difference scheme. Note that the velocity disturbance in Eqs. (3) and (4) is added in each time step from $t = 0$ to $t = \pi$ with the time interval $\Delta t = 10^{-3}$. The imposed disturbance with a negligible divergence, with the maximum local value on the order of A_0, is projected onto the divergence-free space by solving the pressure Poisson equation in each time step.

In the spatial discretization, grid points are uniform in the streamwise and azimuthal directions, and exponentially stretched grid points

$$r_j = \frac{\tanh\left[b(j-1)/(N_r-1)\right]}{\tanh b}R, \quad j = 1, 2, \ldots, N_r \tag{6}$$

with $b = 2$ are used in the radial direction. Cases V4, V8, and V12 in Table I with the same Re and different initial disturbances have transitioned to fully developed turbulence. The spatial resolution is examined by grid convergence tests in Appendix B and resolution quantifications in the fully developed turbulent state. The distance $y = R - r$ from the wall is normalized by the viscous length scale $\delta_\nu = \nu/u_\tau$ as $y^+ = y/\delta_\nu$, where the superscript "+" refers to a quantity normalized by u_τ and $u_\tau = \sqrt{\tau_w/\rho}$ denotes the wall-friction velocity, with the density $\rho = 1$ and the wall shear stress τ_w. In Table I, our resolutions are slightly higher than those in typical pipe DNS studies,[39,40] e.g., the wall-normal grid resolution $\Delta r^+ \le 0.51$ at $y^+ \le 30$ and $\Delta r^+ \le 0.74$ in the viscous wall region at $y^+ \le 50$.

B. VSF method for pipe flows

The VSF is a Lagrangian-based identification method of coherent flow structures.[36] The VSF ϕ_v, a globally smooth scalar field, is defined to satisfy the constraint

$$\boldsymbol{\omega} \cdot \nabla \phi_v = 0, \tag{7}$$

which means every isosurface of ϕ_v is a vortex surface consisting of vortex lines. The VSF evolution is calculated by the two-time method,[49] as a post-processing step based on a time series of velocity-vorticity fields obtained by solving the NS equations. The numerical implementation of the VSF calculation is the same as that detailed in Refs. 25 and 49, except for the extension to cylindrical coordinates.

For the initial velocity in Eq. (3), an exact initial VSF field is $\phi_{v0} = (1 - r/R)^2$, which satisfies the VSF boundary condition. The isosurfaces of ϕ_{v0} are concentric vortex tubes. As sketched in Fig. 3, the initial VSF isosurface of $\phi_v = 0.09$ (blue solid line), corresponding to the tube at $r/R = 0.7$, is perturbed by the radial disturbance (red dashed line) in Eq. (3).

Generally, the computed ϕ_v cannot be an exact VSF solution, and the error is quantified by $\varepsilon_\phi = \langle|\lambda_\omega|\rangle$,[49] where $\lambda_\omega = (\boldsymbol{\omega} \cdot \nabla\phi_v)/(|\boldsymbol{\omega}||\nabla\phi_v|)$ is the cosine of the angle between the vorticity and the VSF gradient and $\langle\cdot\rangle$ denotes the volume average over Ω. The VSF

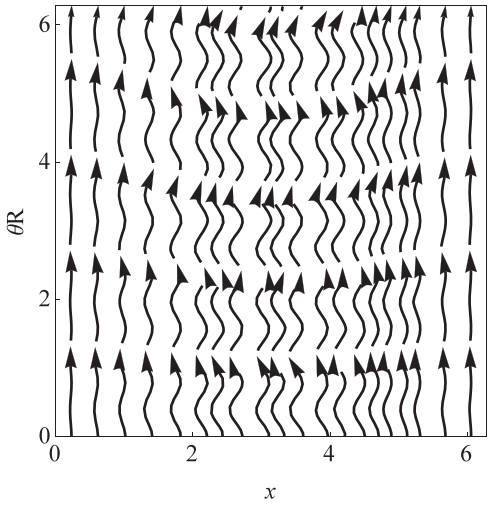

FIG. 2. Vortex lines integrated from Eq. (5) with $A = A_0 \times 10^4$ and $m = 8$ on the x–θ plane (expanded from the tube surface) at $r = R$.

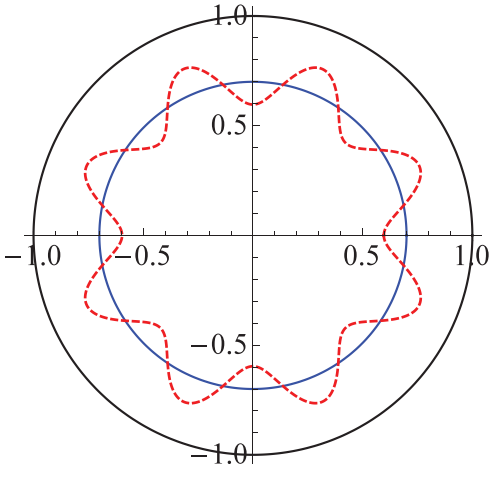

FIG. 3. Sketch of the initial VSF isosurface (blue solid line) and the radial velocity disturbance (red dashed line) in the r–θ plane.

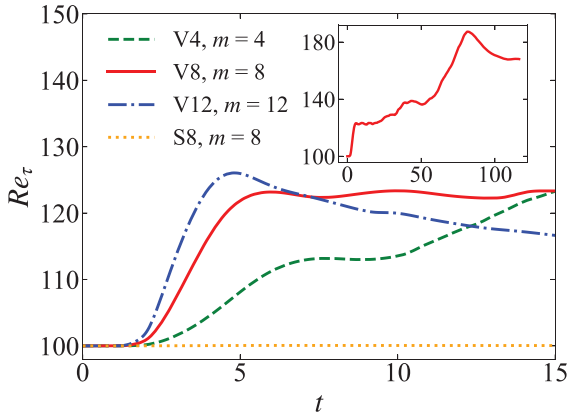

FIG. 4. Temporal evolution of the wall-friction Reynolds number in various DNS cases.

calculation is applied to the early stage of the transition at $0 \le t \le 15$, and the error is very small as $\varepsilon_\phi < 4\%$.

III. RESULTS

A. Flow statistics

The volume-averaged wall-friction Reynolds number $Re_\tau = \langle u_\tau \rangle R/\nu$ is calculated to monitor the transition process. In Fig. 4, Re_τ first surges from $t = 0$ to 5 in cases V4, V8, and V12, signaling the incipient transition, and then it keeps growing with large fluctuations. At later times, it reaches a statistical stationary stage around $Re_\tau = 170$ after $t = 100$ in the inset plot, indicating the fully developed turbulent state. We will focus on case V8 with $m = 8$ in the early transition below, and other cases in Table I are discussed in Appendix A.

The severe deformation of vortex surfaces is associated with the growth of the local friction coefficient $C_f = 2\tau_w/(\rho U_b^2)$, which is proportional to Re_τ. In Fig. 5, the peak of C_f rises from $t = 0$ to 6 and gradually decays with time, and the region of large C_f migrates and elongates along the x-direction. This intensified and growing disturbance region, which triggers the further transition to turbulence, is also represented by the variation of the mean streamwise velocity.

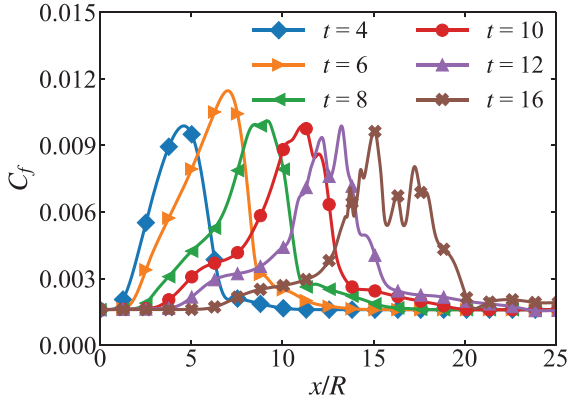

FIG. 5. Temporal evolution of the friction coefficient along the streamwise direction in case V8.

In the early transition at $t = 4$, Fig. 6 shows that $\langle u_x \rangle$ begins to be disturbed from the laminar velocity profile within the core region at $y/R > 0.5$ and at the leading edge around $x = 8$. Within the disturbance region, the variation of $\langle u_x \rangle$ extends toward the wall region, and the profile of $\langle u_x \rangle$ has a clear inflection point. The significant streamwise acceleration in the near-wall region around $x = 4$ causes the large C_f in Fig. 5. This disturbance gradually weakens at the tailing edge around $x = 2$.

The vorticity evolution is characterized by enstrophy components $\Omega_x = \langle \omega_x^2 \rangle/2$, $\Omega_r = \langle \omega_r^2 \rangle/2$, and $\Omega_\theta = \langle \omega_\theta^2 \rangle/2$. In case V8, enstrophy components grow rapidly from $t = 2$, and radial and azimuthal components peak around $t = 5$; in case S8, the enstrophy growth is much milder and decays soon. The variation of the enstrophy is closely related to the geometry of vortex surfaces, which will be discussed in detail below.

B. Deformation of wall-parallel vortex surfaces

The temporal evolution of the VSF isosurface of $\phi_v = 0.09$ color-coded by r/R in the pipe transition with $m = 8$ is shown in Fig. 7. This isosurface corresponds to the initial one at $r = 0.7R$ near the wall, as illustrated in Fig. 3. Note that the length scale in the x-direction is artificially compressed by a factor of two in Fig. 7 and the following VSF visualization figures for enhancing the visual effect of radial deformation. Some vortex lines are integrated from points on the isosurfaces, and they are faithfully attached on the surfaces with the negligible VSF error ε_v.

At the early time $t = 1$, the VSF isosurface remains a smooth tube with little disturbance in Fig. 7(a). Under the temporally and azimuthally fluctuating radial disturbance (see Fig. 3), the vortex surface begins to form bulges[50,51] elongated in the x-direction in Fig. 7(b) at $t = 2$. The number of bulges is equal to m in Eq. (3). Then, the bulges gradually evolve into a petal-like, corrugated structure with the increasing height of the wavy part at $t = 3$–4 in Figs. 7(c) and 7(d). The formation of the vortex bulge is consistent with the rapid growth of Ω_r at $t = 2$–4 in Fig. 8(b) and is modeled with the initial disturbance in Appendix C.

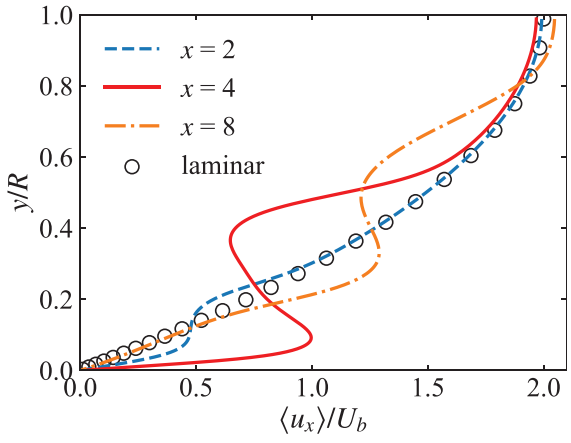

FIG. 6. Mean normalized streamwise velocity profiles (lines) at different streamwise locations at time $t = 4$ in case V8, along with the laminar Poiseuille profile u_x (circles) in Eq. (3).

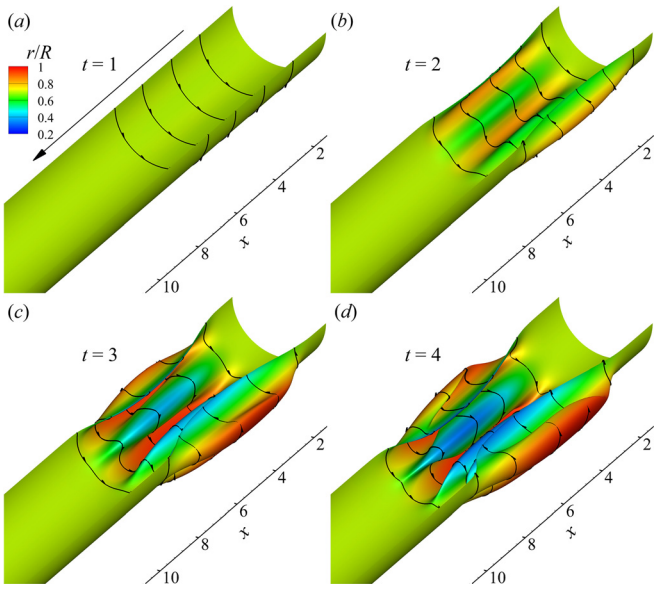

FIG. 7. VSF isosurfaces of $\phi_v = 0.09$ color-coded by r/R at (a) $t = 1$, (b) $t = 2$, (c) $t = 3$, and (d) $t = 4$ in case V8. Some vortex lines are integrated from points on the surfaces.

The geometric deformation of vortex surfaces is quantified by the variation of the volume-averaged VSF gradient magnitude $\langle|\nabla\phi_v|\rangle - \langle|\nabla\phi_{v0}|\rangle$ as Fig. 9 shows. For case V8, the deformation level of VSF isosurfaces surges from $t = 0$ to 6, and then the growth slows down. Around $t = 11$, the deformation rises again, which corresponds to the occurrence of instability of the strong shear layer discussed in Sec. III D. For case S8, the deformation level grows mildly from $t = 0$ to 3 and then decays, because the disturbance of the streamwise velocity streak cannot trigger the pipe flow transition, which is elaborated in Appendix A 2.

Furthermore, we characterize the elevation and descent of two typical VSF isosurfaces.[50] For a given VSF isosurface, the distance y to the wall is calculated at a number of sample points on this surface. The maximum and minimum operators $\max_{\phi_v=c}(\cdot)$ and $\min_{\phi_v=c}(\cdot)$ of y over the whole isosurface of $\phi_v = c$ are defined, respectively, with a constant c. In Fig. 10, the maximum wall distance $\max_{\phi_v=0.09}(y)$ of the VSF isosurface $\phi_v = 0.09$ initially in the wall region rises from 0.3 at $t = 0$ to 0.57 at $t = 3$, and then it grows slowly to reach a stationary

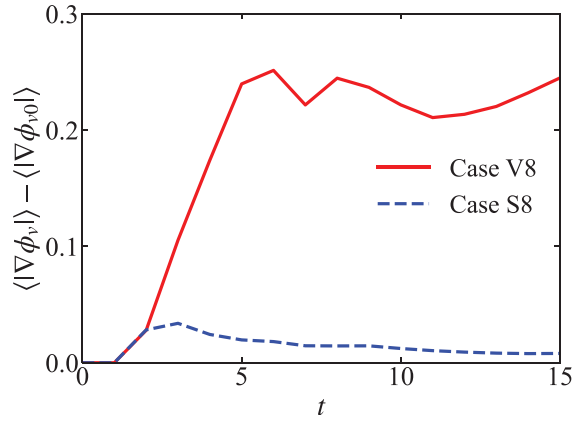

FIG. 9. Temporal evolution of the VSF deformation in cases V8 and S8.

state around 0.7 at $t = 7$. The maximum wall distance of the VSF isosurface $\phi_v = 0.25$ initially near the core region has the same trend. Meanwhile, the minimum wall distance of these two typical VSF isosurfaces shows similar descent trends, i.e., falling first and then relaxing to the location very close to the wall. The continuous corrugated deformation illustrated in Fig. 8 causes the vortex surfaces initially separated in near-wall and core regions to approach and even interlace with each other, and they cover the radial range from 20% at $t = 0$ to 70% at $t = 10$.

As illustrated in Fig. 11, the elevation and descent of vortex surfaces are accompanied by the strong momentum exchange[50] and the generation of streamwise vortex pairs. The streamwise vortex pairs lift-up the near-wall low-speed fluid between them and sweep down the high-speed fluid from the core region toward to the wall, generating streaks of low and high streamwise velocities.[52] The low- and high-speed streaks are alternately arranged in the θ-direction at $\theta = k\pi/m$, $k = 0, 1, \ldots$, as implied by Eq. (C5) from the initial disturbance. The streak positions are the same as those of the raised and sunken parts of the corrugated vortex tube. Each streamwise vortex pair leads to the momentum exchange in the r-direction, causing the growth of C_f and inflection points of $\langle u_x\rangle$ in the r-direction in Figs. 5 and 6. Moreover, the collapse of vortex surfaces within the region of large ω_θ in Fig. 12 indicates the generation of a strong shear layer as the lifted-up low-speed streak meets the incoming high-speed laminar flow upstream.

In Fig. 13, the petal-like corrugated structure propagates and elongates in the streamwise direction at $t = 5$–8, with the increasing

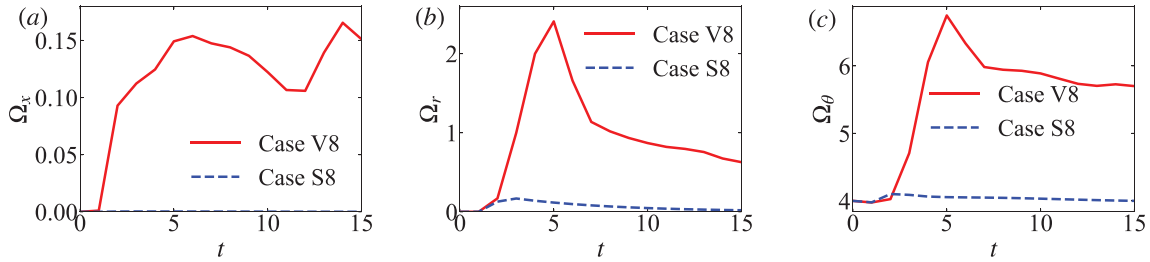

FIG. 8. Temporal evolution of enstrophy components (a) Ω_x, (b) Ω_r, and (c) Ω_θ in cases V8 and S8.

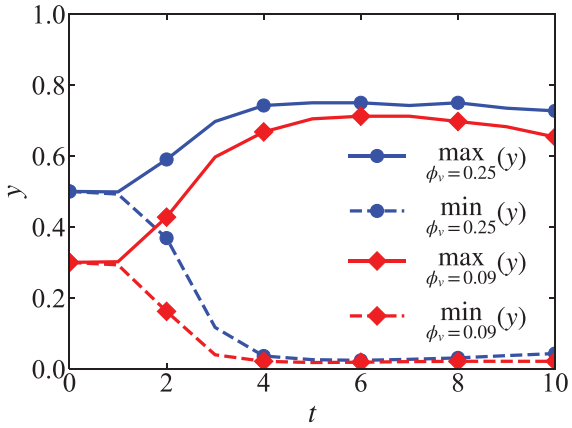

FIG. 10. Temporal evolution of the wall distances of two typical VSF isosurfaces.

length between the leading and trailing edges. In the meantime, the bulge heads grow and converge to the pipe centerline, and then roll up in the r–θ plane. In Fig. 13(d) at time $t=8$, the head at the leading edge accelerates to form a sharp tip, which is similar to the formation of the triangular bulge in transitional channel flows[50] and boundary layers[37] due to the larger y and u_x in shear flows. In addition, the gradual transition with a clear process of vortex formation is similar to the pipe flow transition with a weak turbulence disturbance near the inlet.[20]

C. Formation of streamwise helical vortex loops

The rolling up of vortex bulges in Fig. 13 is along with the generation of streamwise vortices. Next, we elucidate how the initial vortex loops in the r–θ plane with very small streamwise vorticity components ($\omega_x \ll \omega_\theta$ at $t=0$) form streamwise helical vortex loops elongated in the x-direction via a series of successive vortex reconnections.

The top view at $t=4$ in Fig. 14(a) shows the streamwise stretching of vortex loops attached on a VSF isosurface due to the difference

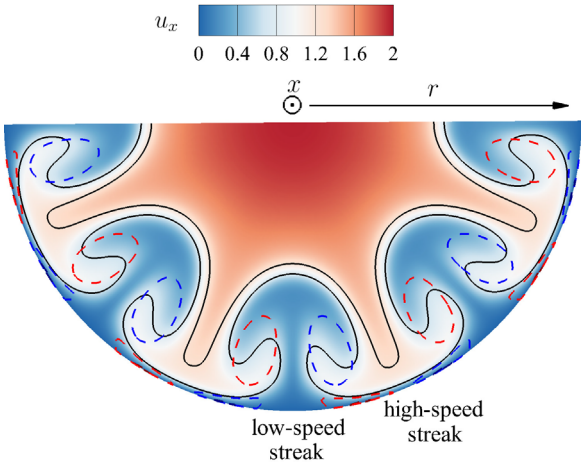

FIG. 11. Contour of u_x, VSF isolines of $\phi_v = 0.04$ and 0.16 (black solid lines from bottom to top), and isolines of $\omega_x = -3$ (blue dashed lines) and $\omega_x = 3$ (red dashed lines) on the r–θ plane at $t=4$ and $x=2.82$ in case V8.

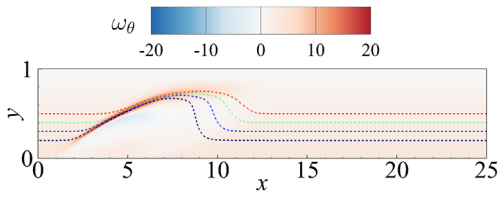

FIG. 12. Contour of ω_θ and VSF isolines of $\phi_v = 0.04$, 0.09, 0.16, and 0.25 (dashed lines from bottom to top) on the x–y plane at $\theta=0$ and at $t=4$ in case V8.

of u_x in the r-direction, which generates m streamwise vortex pairs with moderate ω_x in Fig. 11. The rolling up of the vortex pairs form highly coiled vortex loops attached on the corrugated vortex tube in Fig. 14(b).

At $t=5$, the highly coiling part on the leading edge of petal-like vortex lines in Fig. 15(a) has self-reconnection with the viscous cancelation mechanism[21] at the neck of a petal-like vortex loop. Subsequently, m secondary vortex loops, the red ones in Fig. 15(b), pinch off. We remark that the self-reconnection, during the converging of petal-like vortex loops toward the pipe centerline, was not observed in the transitions in channel flow[25] and boundary layer,[37] because this evolution under the azimuthal symmetry is distinguished from those in the other two canonical wall-bounded flows.

Then at $t=5.02$ in Fig. 16, the detached secondary vortex ring (red) in Fig. 15(b) is captured and further reconnected with another detached secondary vortex ring (blue) from a highly coiled vortex loop upstream. This reconnection forms a streamwise elongated vortex loop (red) in Fig. 16(b). In the subsequent evolution, the helical vortex loops keep growing in the x-direction through stretching and reconnection.

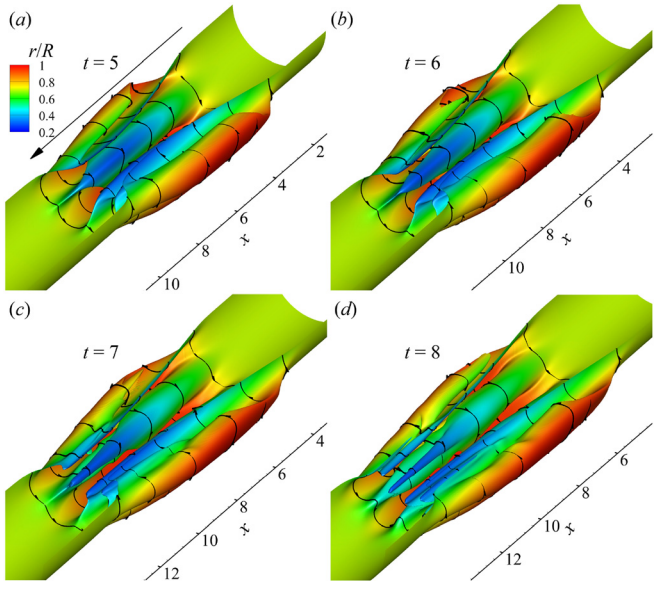

FIG. 13. VSF isosurfaces of $\phi_v = 0.09$ color-coded by r/R at (a) $t=5$, (b) $t=6$, (c) $t=7$, and (d) $t=8$ in case V8. Some vortex lines are integrated from points on the surfaces.

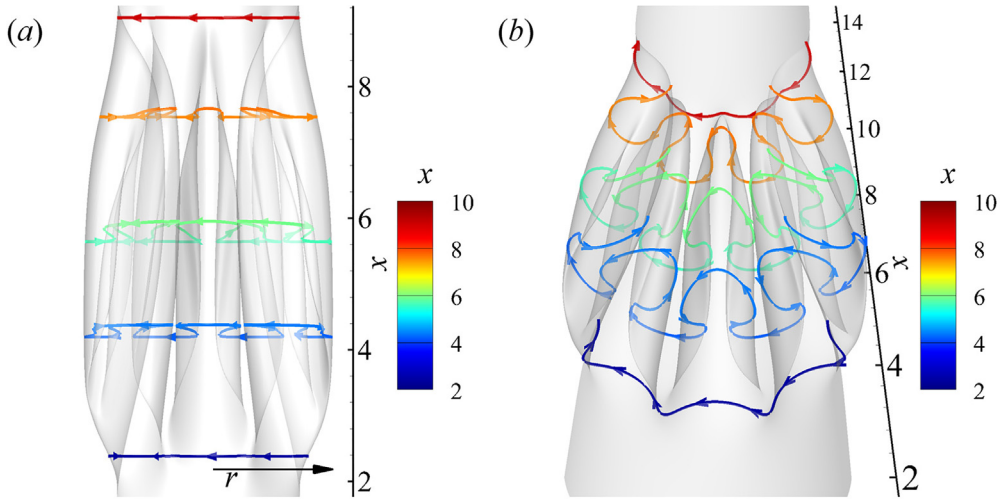

FIG. 14. (a) Top view and (b) perspective view of the VSF isosurface of $\phi_v = 0.09$ (translucent) and typical vortex lines (color-coded by x) integrated from points on the surface at $t = 4$ in case V8.

Furthermore, at $t = 5.04$ in Fig. 17(a), the rear part of the leading streamwise elongated vortex loop (red) can be reconnected with the front part of the trailing coiled vortex loop (blue) shown in Fig. 14. This type of reconnection also forms a long streamwise helical vortex loop (red) and a new petal-like vortex loop (blue) in Fig. 17(b), and its mechanism is sketched in Fig. 18 to illustrate a streamwise growing mechanism of vortex loops. The successive reconnections (similar to the greedy snake) shown in Figs. 15–17 make the streamwise helical vortex loops growing rapidly in the x-direction.

The streamwise helical vortex loop in Fig. 17(b) spans from about $x = 4.5$ to $x = 10.5$, almost throughout the disturbance region with corrugated vortex surfaces in Fig. 13(a). Its wall distance spans from $y = 0.035$ near the wall to $y = 0.49$ near the core region, attached on the different vortex surfaces with a range of initial wall distances. Thus, the streamwise length scale of the long helical vortex loops rises from R at $t = 5$ in Fig. 15 to $6R$ at $t = 5.04$ in Fig. 17(b). The formation of streamwise helical vortex loops around $t = 5$ is accompanied by the notable growth of Ω_x in Fig. 8(a), i.e., the generation of streamwise vortices.

The generation of the streamwise helical vortex loops continues to form strong local vortex cores. At a later time $t = 8$, Fig. 19 depicts that each streamwise helical loop coils around a pair of streamwise vortex cores. The vortex cores identified by the Q criterion (red) are parts of vortex surfaces identified by the VSF isosurface $\phi_v = 0.35$ (gray). Two strands of each streamwise helical vortex loop have opposite chirality of coiling. The streamwise vortex pairs alternately along the azimuthal direction can be the optimal disturbance to achieve the maximum transient growth and promote the bypass transition of pipe flows.[53–55]

D. Elongation and breakdown of streamwise helical vortex loops

The streamwise helical vortex loops elongate via successive reconnections and move downstream. This process is characterized by

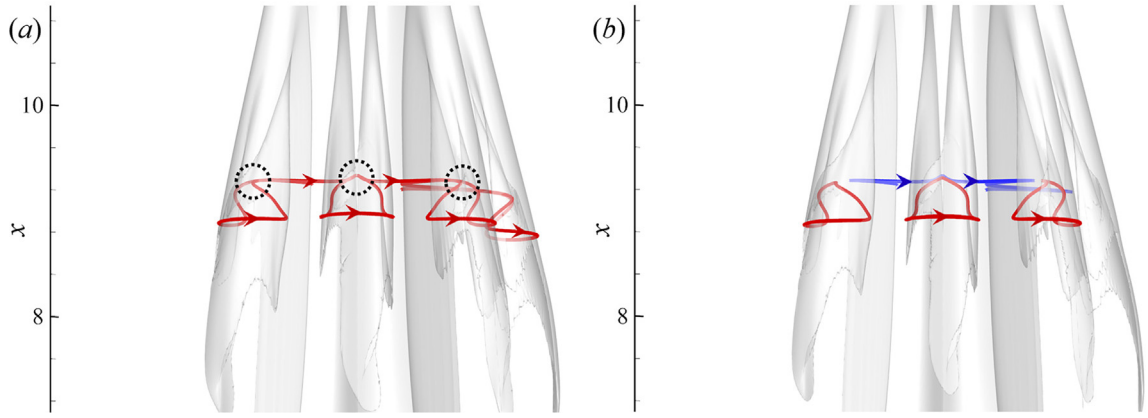

FIG. 15. Self-reconnection of a highly stretched and coiled vortex loop at $t = 5$ in case V8; (a) before and (b) after reconnection. The reconnection locations are marked by dashed circles. The vortex loops are integrated from points on the VSF isosurface of $\phi_v = 0.35$ (translucent).

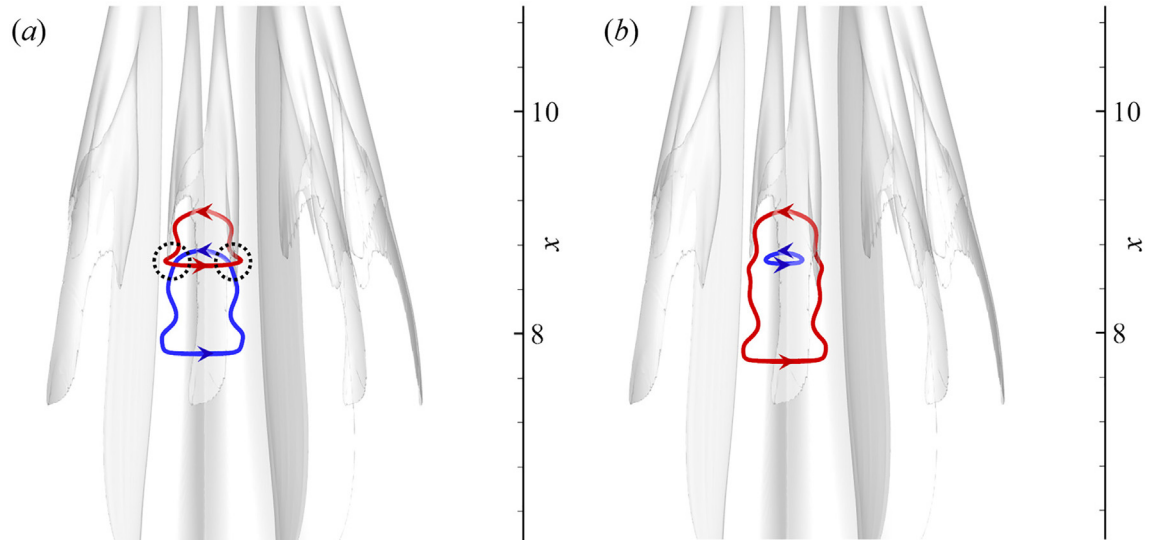

FIG. 16. Reconnection of two pinched-off secondary vortex loops at $t = 5.02$ in case V8; (a) before and (b) after reconnection. The reconnection locations are marked by dashed circles. The vortex loops are integrated from points on the VSF isosurface of $\phi_v = 0.35$ (translucent).

tracing the position of the leading and trailing edges of the streamwise helical loops. As depicted in Fig. 20, we identify the streamwise helical vortex structure by integrating a cluster of vortex lines on the VSF isosurfaces. The leading-edge position x_{LE} and trailing-edge position x_{TE} are defined by the largest and smallest values of x, respectively, in the cluster of vortex lines at a given time. The vortex loops containing x_{LE} and x_{TE} are colored in red and blue in Fig. 20, respectively.

Figure 21 plots the temporal evolution of x_{LE} and x_{TE} and the length $x_{LE} - x_{TE}$ of streamwise helical loops, along with their linear fits at $5 \leq t \leq 9$. After the formation of helical vortex loops at $t = 5$, both x_{LE} and x_{TE} move downstream. The leading edge moves faster than the trailing edge, leading to the steady elongation of the streamwise vortical structures. The propagation speeds of U_{LE} and U_{TE} of leading and trailing edges are estimated from the linear fits in Fig. 21. The normalized results $U_{LE}/U_b = 1.62$ and $U_{TE}/U_b = 0.58$ show that the leading edge moves faster and the trailing edge moves slower than the mean flow, which is similar to the motion of slug structures in the later stage of pipe transition.[14]

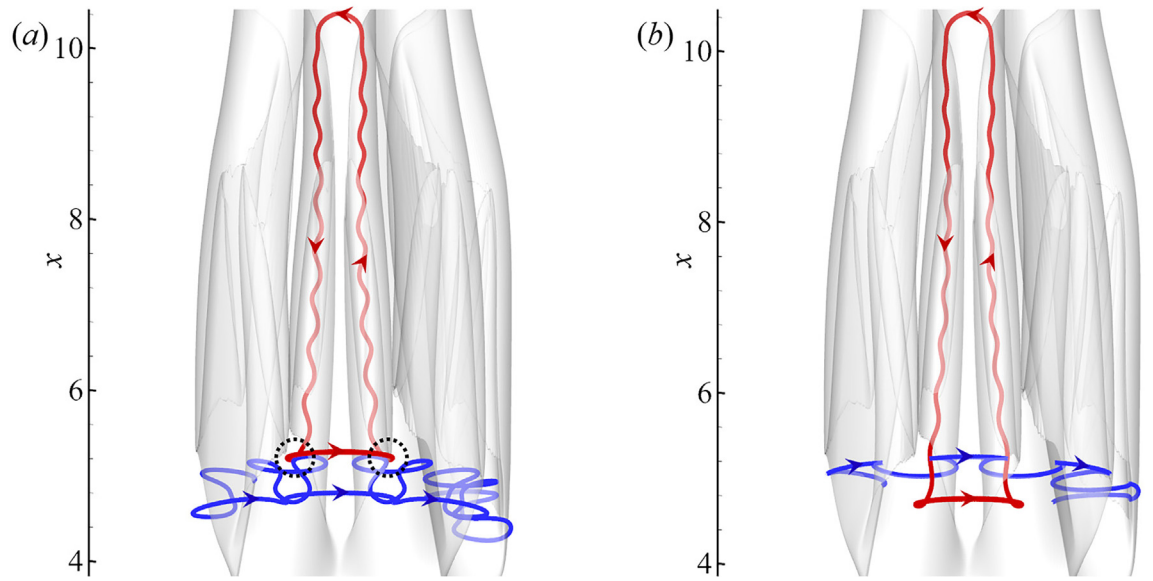

FIG. 17. Reconnection of the streamwise helical loop and stretched and coiled vortex loops at $t = 5.04$ in case V8; (a) before and (b) after reconnection. The reconnection locations are marked by dashed circles. The vortex loops are integrated from points on the VSF isosurface of $\phi_v = 0.08$ (translucent).

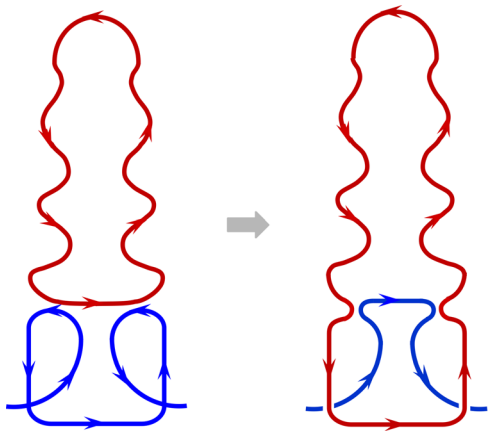

FIG. 18. Schematics of the vortex reconnection in Fig. 17.

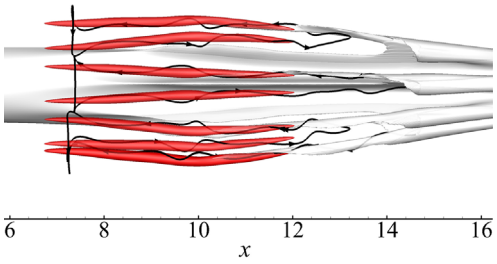

FIG. 19. Streamwise helical vortex loops integrated from points on the VSF isosurface of $\phi_v = 0.35$ (gray) and the isosurface of the Q-criterion (red) at $t = 8$ in case V8.

Around $t = 10$, the growth of streamwise loops slows down, and then, around $t = 12$, the streamwise loops begin to be shortened due to the breakdown of the trailing edge caused by the Kelvin–Helmholtz (KH) instability of shear layers. In Fig. 22, the petal-like deformation and the generation of streamwise helical vortex loops introduce three-dimensional characteristics to vortex surfaces, and small-scale wrinkled or helical structures emerge at $t = 9$–12.

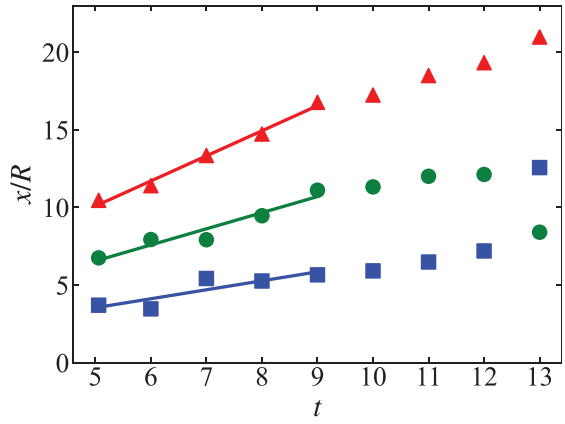

FIG. 21. Temporal evolution of x_{LE} (triangles), x_{TE} (squares), and $x_{LE} - x_{TE}$ (circles) of the cluster of streamwise helical loops along with their linear fits (solid lines).

The arched part of the corrugated vortex surface in Fig. 13(d) at $t = 8$ corresponds to a low-speed streak, and its trailing edge becomes unstable at $t = 10$ in Fig. 22(a). From the side view in Fig. 23, the vortex surfaces are rolled up via the KH instability of the strong shear layer, which is characterized by large ω_θ and formed by the elevation and descent of vortex surfaces (also refer to Fig. 12). Then, small-scale turbulent-like structures are produced at the trailing edge, and they propagate downstream faster than the leading edge of the corrugated vortical structure (see Fig. 21 after $t = 12$).[56] The breakdown of the trailing edge of the helical vortex loops also enhances Ω_x in Fig. 8(a) and VSF deformation in Fig. 9, and triggers the varicose mode instability of streaks, leading to the expansion and contraction of the vortical structures along the x-direction and the emergence of turbulent spots.[57,58]

IV. CONCLUSIONS

We extend the VSF method to investigate the evolution of vortex surfaces in temporally evolving transitional pipe flows. In particular, we identify and characterize the vortex reconnection in the formation of streamwise helical vortex loops in the early stage of the pipe transition. In the DNS of pipe flows, a slow time-varying, blow-and-suction disturbance is imposed on laminar Poiseuille flow to trigger a relatively

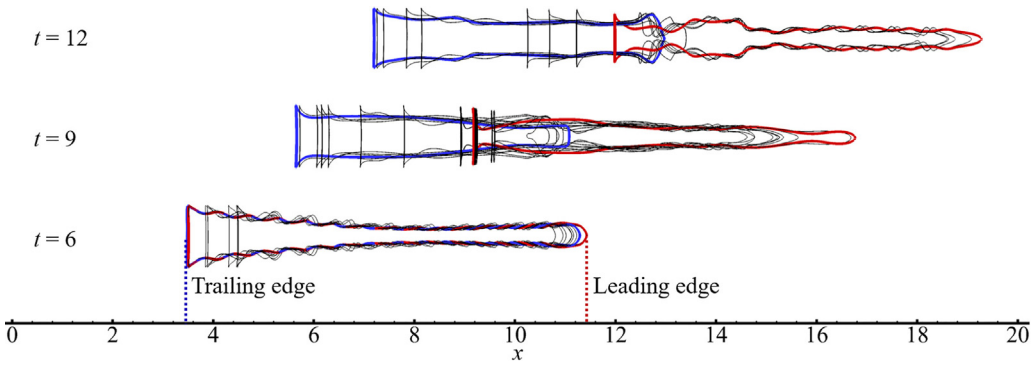

FIG. 20. Top view of the propagation and elongation of a cluster of streamwise helical vortex loops at different times in case V8. Red and blue loops contain x_{LE} and x_{TE}, respectively.

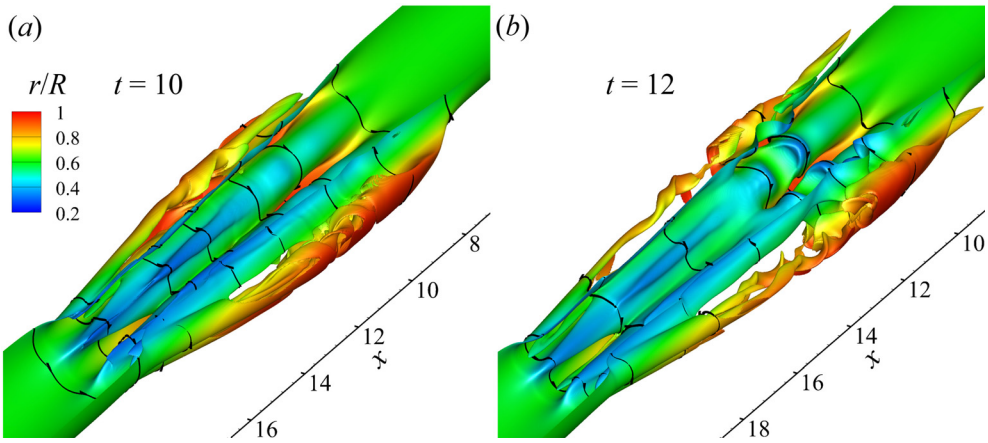

FIG. 22. VSF isosurfaces of $\phi_v = 0.16$ color-coded by r/R at (a) $t = 10$ and (b) $t = 12$ in case V8. Some vortex lines are integrated from points on the surfaces.

mild transition with a clear evolution process of vortical structures. The initial velocity field has an exact VSF solution whose isosurfaces are wall-parallel concentric tubes consisting of sinuous vortex loops. The VSF evolution is calculated by the two-time method.[25,49]

Under the initial disturbance of velocities in alternating plus and minus r-directions in case V8, the vortex surfaces first become corrugated with m streamwise elongated bulges at $t = 0$–4. The escalation and descent of vortex surfaces characterize high- and low-speed streaks and streamwise vortex pairs, rolling up the closed vortex loops into highly coiled ones. The deformation of vortex surfaces enhances momentum exchange in the r-direction and causes the surge of the wall-friction coefficient. In particular, the difference of u_x on the vortex surface stretches the vortex loops in the x-direction, introducing strong three-dimensional characteristics on the vortex loops initially lying on the r–θ plane.

At $t = 5$–8, the stretched coiled vortex loops reconnect with each other at the head and tail with the viscous cancelation mechanism. First, streamwise helical vortex loops spanning R in the x-direction are generated at the tailing edge of the corrugated vortex surfaces. In the meantime, the self-reconnection occurs at the head of the streamwise helical vortex loops, and then small secondary vortex rings pinch off. Then, the streamwise helical vortex loop reconnects with the secondary vortex ring to grow in the streamwise direction via successive vortex reconnections. This greedy snake mechanism makes the helical vortex loops growing rapidly. The long loops span $11R$ from the trailing edge to the leading edge in the x-direction at $t = 9$.

The elevation of vortex surfaces also generates strong shear layers at the trailing edge of the corrugated structure. Around $t = 10$, the KH instability of the shear layer breaks down the trailing edge of the streamwise helical vortex loops into small-scale structures, which further triggers a varicose mode instability to form turbulent spots.

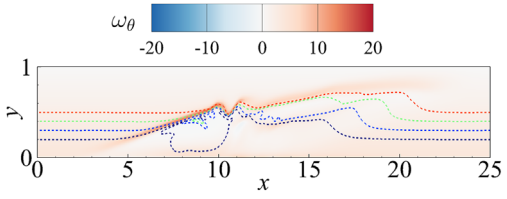

FIG. 23. Contour of ω_θ and VSF isolines of $\phi_v = 0.04$, 0.09, 0.16, and 0.25 (dashed lines from bottom to top) on the x–y plane at $\theta = 0$ and at $t = 10$ in case V8.

The generation of streamwise helical vortex loops via successive reconnections can be found with various A_0 and m in the initial disturbance in Eq. (3) and at a range of Re in Appendix A 1. On the other hand, it is not found for the initial disturbance with imposed streaks in Appendix A 2. The lack of the generation of streamwise vortex loops can inhibit the transition in case S8.

In future work, we will explore whether this successive reconnection mechanism exists in the later transition stage with more complex initial disturbances. Furthermore, the VSF method can be applied to study the self-sustained process[59] and the relative equilibrium state of traveling wave solutions[60–63] in pipe flows.

ACKNOWLEDGMENTS

This work has been supported in part by the National Key R&D Program of China (Grant No. 2020YFE0204200), the National Natural Science Foundation of China (Grant Nos. 11925201, 91541204, and 11988102), the National Numerical Wind Tunnel Project of China (Grant No. NNW2021ZT6-B36), and the Xplore Prize.

AUTHOR DECLARATIONS

Conflict of Interest

The authors have no conflicts to disclose.

DATA AVAILABILITY

The data that support the findings of this study are available from the corresponding author upon reasonable request.

APPENDIX A: EFFECTS OF THE INITIAL CONDITION ON VSF EVOLUTION

1. Azimuthal wavenumber in the initial disturbance

We vary the parameters of the initial wavy disturbance in Eqs. (3) and (4) to study the influence of the initial disturbance on the

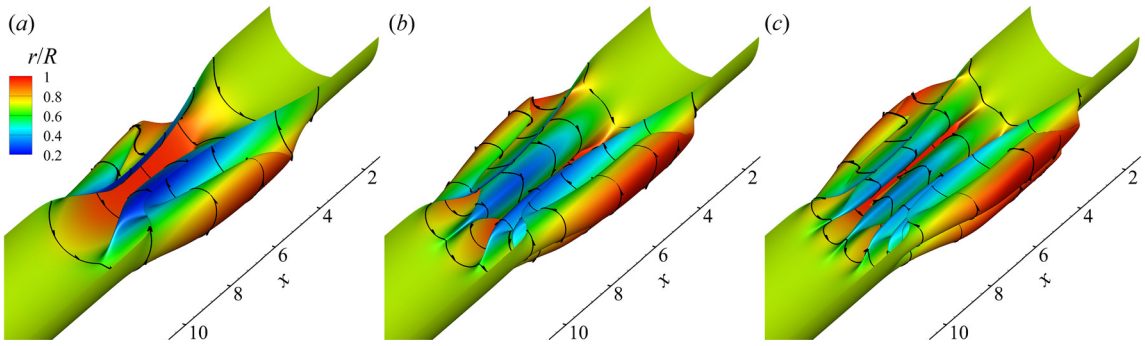

FIG. 24. The comparison of VSF isosurfaces at time $t = 5$ with (a) $m = 4$, (b) $m = 8$, and (c) $m = 12$ in cases V4, V8, and V12, respectively. The VSF isosurface of $\phi_v = 0.09$ is color-coded by r/R. Some vortex lines are integrated from points on the surfaces.

transition process and the evolution of vortex surfaces. First, the number of bulges in the vortex surface deformation is equal to m in Fig. 24, and the surge of Re_τ occurs earlier and the growth is stronger for larger m in Fig. 4. From the VSF isocontour lines with $m = 4$ (green dashed line), 8 (red solid line), and 12 (blue dash-dotted line) on a cross section at $t = 5$ in Fig. 25, the petal structures are closer to each other for larger m. The approaching petal structures can have intensified vortex interactions[38] and cause strong growth of C_f at $t \leq 5$. On the other hand, the heads of petals for $m = 4$ are closest in Fig. 25, which appears to trigger the strongest vortex interaction and the growth of Re_τ at the later time period $t = 10-15$ in Fig. 4. Moreover, the deformation of vortex surfaces can be intensified by increasing A_0 in Eq. (4).

Second, the formation of streamwise helical vortex loops as a robust evolutionary feature is consistently observed for various m and Re. The loops are narrower in the θ-direction and shorter in the x-direction for larger m (not shown). Besides the transition cases, the loop formation is also observed at low $Re = 2000$, in which the flow is relaminarized after a short transitional period.

2. Disturbance on the streamwise velocity component

The velocity disturbance in Eq. (3) for cases V4, V8, and V12 is imposed on the radial velocity, which produces the streamwise vorticity. In case S8, the same disturbance is switched to the streamwise velocity as

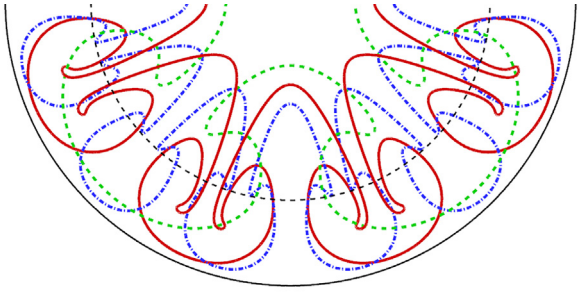

FIG. 25. VSF isolines with $m = 4$ (green dashed line), $m = 8$ (red solid line), and $m = 12$ (blue dash dot line) in cases V4, V8, and V12, respectively. The isolines are on the r–θ plane at $x = 7.81$ and at $t = 5$, along with $r = 0.7R$ (black dashed line).

$$u_x = 2U_b\left(1 - \frac{r^2}{R^2}\right) - A(t)\frac{r}{R}\cos(m\theta)\sin\left(\frac{x}{2}\right), \quad u_r = 0, \quad u_\theta = 0 \tag{A1}$$

with $m = 8$ and the same $A(t)$ in Eq. (4). The form of Eq. (A1) represents alternating low- and high-speed streaks of u_x. More DNS parameters are listed in Table I. The corresponding initial vorticity is

$$\omega_x = 0, \quad \omega_r = \frac{Am}{R}\sin\left(\frac{x}{2}\right)\sin(m\theta), \quad \omega_\theta = \frac{4rU_b}{R^2} + \frac{A}{R}\sin\left(\frac{x}{2}\right)\cos(m\theta), \tag{A2}$$

which implies that all vortex lines form eight-petal loops in the r–θ plane.

From the inviscid vorticity equation with Eqs. (A1) and (A2) at the initial time, the vortex lines are only stretched in the x-direction in case S8 instead of the r-direction in case V8. The lack of the persistent stretching mechanism in Eq. (C4) causes much milder growth of Ω_r in case S8 than that in case V8 in Fig. 8(b).

The evolution of VSF isosurfaces in Fig. 26 shows that the initially corrugated vortex surface under the disturbance in Eq. (A1) does not persistently grow in the r-direction. The lack of a large enough difference of u_x on the corrugated structure does not trigger the formation of streamwise helical vortex loops in Fig. 19, and Ω_x in case S8 only has very weak growth and then quickly decays. Thus, the transition in case S8 does not occur with negligible growth of Re_τ in Fig. 4. It is consistent that the VSF deformation for case S8 is much weaker than that for case V8 in Fig. 9.

APPENDIX B: GRID CONVERGENCE TEST

The grid convergence of the DNS is examined by conducting three simulations on different numbers of grid points $[N_x, N_r, N_\theta] = [450, 64, 128]$, (900, 128, 256), and (1800, 256, 512). Typical statistics, the wall-friction Reynolds number and the mean normalized streamwise velocity, in the three simulations are compared in Fig. 27. Both quantities converge for the gird $[N_x, N_r, N_\theta] = [1800, 256, 512]$, which is used in case V8 (see Table I). Moreover, it is confirmed that the profile of $\langle u_x^+ \rangle$ in the fully

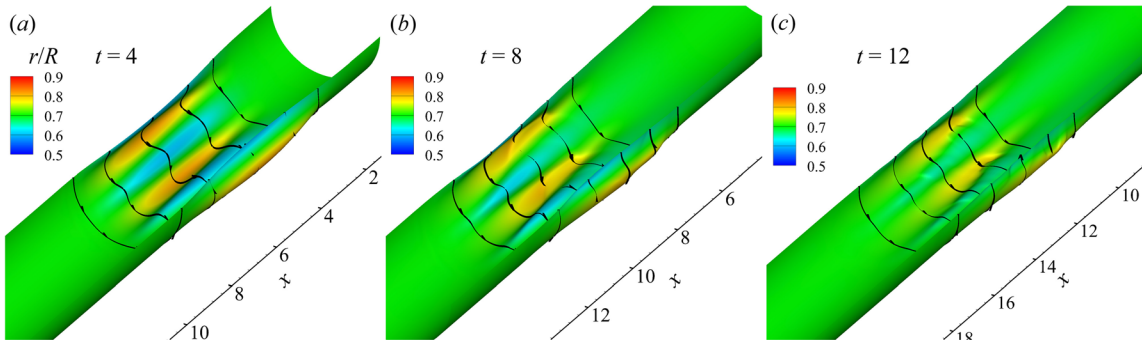

FIG. 26. VSF isosurfaces of $\phi_v = 0.09$ color-coded by r/R at (a) $t = 4$, (b) $t = 8$, and (c) $t = 12$ in case S8. Some vortex lines are integrated from points on the surfaces.

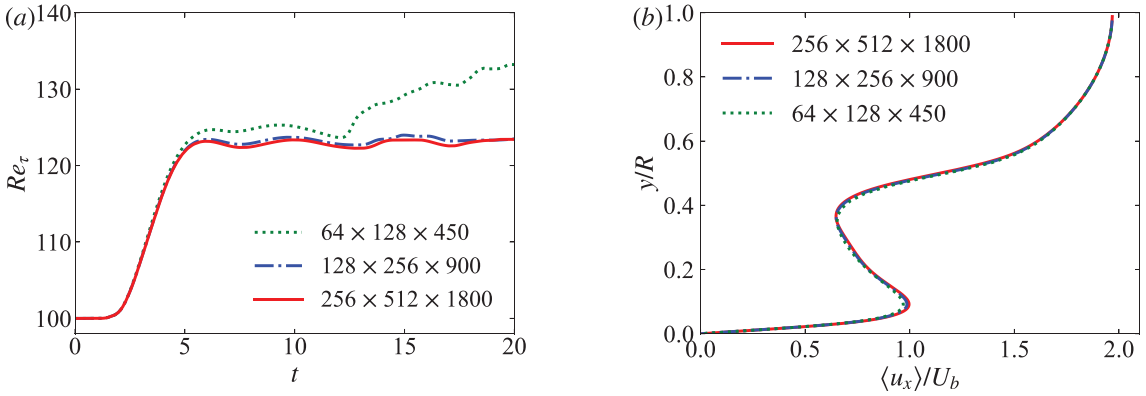

FIG. 27. Grid convergence test with different grid resolutions with $Re = 5000$ and $m = 8$. (a) Temporal evolution of the wall-friction Reynolds number; (b) mean normalized streamwise velocity profile at $x = 4$ and $t = 4$.

developed turbulent state agrees well with the DNS result of Wu and Moin[39] (not shown).

APPENDIX C: MODELING OF INITIAL VORTEX-SURFACE DEFORMATION

Substituting the initial velocity in Eq. (3) and the initial vorticity in Eq. (5) into the vorticity equation $\mathrm{D}\boldsymbol{\omega}/\mathrm{D}t = (\boldsymbol{\omega}\cdot\nabla)\boldsymbol{u}$, where the viscous term is neglected for high-Re flow, we obtain vorticity component equations $\mathrm{D}\omega_x/\mathrm{D}t = 0$, $\mathrm{D}\omega_\theta/\mathrm{D}t = 0$, and

$$\frac{\mathrm{D}\omega_r}{\mathrm{D}t} = \frac{4mArU_b}{R^3}\sin(m\theta)\sin\left(\frac{x}{2}\right) \tag{C1}$$

at the initial time. After a short time $t = \Delta T$, we approximate

$$\omega_r = \frac{4mArU_b}{R^3}\sin(m\theta)\sin\left(\frac{x}{2}\right)\Delta T \tag{C2}$$

by integrating Eq. (C1) in a Lagrangian view, suggesting that the initial concentric vortex loops mainly deform in the radial direction.

We assume ω_x and ω_θ have little change from $t = 0$ to ΔT, and take $x = \pi$, where the vortex surface has the maximum deformation, and then obtain

$$\omega_x = 0, \quad \omega_r = \frac{4mAU_b\sin(m\theta)}{R^3}r\Delta T, \quad \omega_\theta = \frac{4U_b}{R^2}r. \tag{C3}$$

At $t = \Delta T$, the geometry of VSF isosurfaces is determined by the VSF constraint in Eq. (7). It is equivalent to solve the characteristic equation $\mathrm{d}r/\omega_r = r\mathrm{d}\theta/\omega_\theta$ of the vorticity,[64] and its solution

$$r(\theta, \Delta T) = r_0\exp\left[-\frac{A\Delta t}{R}\cos(m\theta)\right] \tag{C4}$$

estimates the radial position of a VSF isosurface with the initial radial position at r_0. This approximation suggests the rapid radial deformation of vortex surfaces in the initial short time period. The maximum radial deformation, indicating the location of streaks, occurs at

$$\theta = \frac{k\pi}{m}, \quad k = 0, 1, 2, \ldots. \tag{C5}$$

REFERENCES

[1]O. Reynolds, "An experimental investigation of the circumstances which determine whether the motion of water shall be direct or sinuous, and of the law of resistance in parallel channels," Proc. R. Soc. London **35**, 84–99 (1883).
[2]H. Choi, P. Moin, and J. Kim, "Active turbulence control for drag reduction in wall-bounded flows," J. Fluid Mech. **262**, 75–110 (1994).

[3]A. P. Willis, Y. Hwang, and C. Cossu, "Optimally amplified large-scale streaks and drag reduction in turbulent pipe flow," Phys. Rev. E **82**, 036321 (2010).
[4]B. Eckhardt, T. M. Schneider, B. Hof, and J. Westerweel, "Turbulence transition in pipe flow," Annu. Rev. Fluid Mech. **39**, 447–468 (2007).
[5]T. M. Schneider, B. Eckhardt, and J. A. Yorke, "Turbulence transition and the edge of chaos in pipe flow," Phys. Rev. Lett. **99**, 034502 (2007).
[6]F. Mellibovsky, A. Meseguer, T. M. Schneider, and B. Eckhardt, "Transition in localized pipe flow turbulence," Phys. Rev. Lett. **103**, 054502 (2009).
[7]A. P. Willis and R. R. Kerswell, "Coherent structures in localized and global pipe turbulence," Phys. Rev. Lett. **100**, 124501 (2008).
[8]S. K. Robinson, "Coherent motions in the turbulent boundary layer," Annu. Rev. Fluid Mech. **23**, 601–639 (1991).
[9]H. Salwen, F. W. Cotton, and C. E. Grosch, "Linear stability of Poiseuille flow in a circular pipe," J. Fluid Mech. **98**, 273–284 (1980).
[10]X. Wu, P. Moin, and J.-P. Hickey, "Boundary layer bypass transition," Phys. Fluids **26**, 091104 (2014).
[11]T. Ellingsen and E. Palm, "Stability of linear flow," Phys. Fluids **18**, 487–488 (1975).
[12]L. S. Hultgren and L. H. Gustavsson, "Algebraic growth of disturbances in a laminar boundary layer," Phys. Fluids **24**, 1000–1004 (1981).
[13]S. S. Gopalakrishnan and A. C. Mandal, "Transient growth in a flat plate boundary layer under a stream with uniform shear," Phys. Fluids **33**, 114101 (2021).
[14]I. J. Wygnanski and F. H. Champagne, "On transition in a pipe. Part 1. The origin of puffs and slugs and the flow in a turbulent slug," J. Fluid Mech. **59**, 281–335 (1973).
[15]B. Song, D. Barkley, B. Hof, and M. Avila, "Speed and structure of turbulent fronts in pipe flow," J. Fluid Mech. **813**, 1045–1059 (2017).
[16]V. G. Priymak, "Direct numerical simulation of quasi-equilibrium turbulent puffs in pipe flow," Phys. Fluids **30**, 064102 (2018).
[17]B. Hof, J. Westerweel, T. M. Schneider, and B. Eckhardt, "Finite lifetime of turbulence in shear flows," Natures **443**, 59–62 (2006).
[18]T. Mullin, "Experimental studies of transition to turbulence in a pipe," Annu. Rev. Fluid Mech. **43**, 1–24 (2011).
[19]D. Barkley, "Theoretical perspective on the route to turbulence in a pipe," J. Fluid Mech. **803**, P1 (2016).
[20]X. Wu, P. Moin, R. J. Adrian, and J. R. Baltzer, "Osborne Reynolds pipe flow: Direct simulation from laminar through gradual transition to fully developed turbulence," Proc. Natl. Acad. Sci. **112**, 7920–7924 (2015).
[21]S. Kida and M. Takaoka, "Vortex reconnection," Annu. Rev. Fluid Mech. **26**, 169–189 (1994).
[22]J. Yao and F. Hussain, "Vortex reconnection and turbulence cascade," Annu. Rev. Fluid Mech. **54**, 317–347 (2022).
[23]J. Hu and S. D. Peterson, "The influence of collision angle for viscous vortex reconnection," Phys. Fluids **33**, 093608 (2021).
[24]V. L. Nguyen and V. D. Duong, "Vortex ring-tube reconnection in a viscous fluid," Phys. Fluids **33**, 015122 (2021).
[25]Y. Zhao, Y. Yang, and S. Chen, "Vortex reconnection in the late transition in channel flow," J. Fluid Mech. **802**, R4 (2016).
[26]S. Kida, M. Takaoka, and F. Hussain, "Collision of two vortex rings," J. Fluid Mech. **230**, 583–646 (1991).
[27]P. Chatelain, D. Kivotides, and A. Leonard, "Reconnection of colliding vortex rings," Phys. Rev. Lett. **90**, 054501 (2003).
[28]F. Hussain and H. S. Husain, "Elliptic jets. Part 1. Characteristics of unexcited and excited jets," J. Fluid Mech. **208**, 257–320 (1989).
[29]N. J. Zabusky and M. V. Melander, "Three-dimensional vortex tube reconnection: Morphology for orthogonally-offset tubes," Physica D **37**, 555–562 (1989).
[30]M. V. Melander and F. Hussain, "Cross-linking of two antiparallel vortex tubes," Phys. Fluids A **1**, 633–636 (1989).
[31]A. Pumir and E. Siggia, "Collapsing solutions to the 3-D Euler equations," Phys. Fluids A **2**, 220–241 (1990).
[32]O. N. Boratav, R. B. Pelz, and N. J. Zabusky, "Reconnection in orthogonally interacting vortex tubes: Direct numerical simulations and quantifications," Phys. Fluids **4**, 581–605 (1992).
[33]S. Kida and M. Takaoka, "Bridging in vortex reconnection," Phys. Fluids **30**, 2911–2914 (1987).
[34]D. Kleckner and W. T. M. Irvine, "Creation and dynamics of knotted vortices," Nat. Phys. **9**, 253–258 (2013).
[35]S. Xiong and Y. Yang, "Construction of knotted vortex tubes with the writhe-dependent helicity," Phys. Fluids **31**, 047101 (2019).
[36]Y. Yang and D. I. Pullin, "On Lagrangian and vortex-surface fields for flows with Taylor–Green and Kida–Pelz initial conditions," J. Fluid Mech. **661**, 446–481 (2010).
[37]Y. Zhao, S. Xiong, Y. Yang, and S. Chen, "Sinuous distortion of vortex surfaces in the lateral growth of turbulent spots," Phys. Rev. Fluids **3**, 074701 (2018).
[38]S. Xiong, J. You, S. Ruan, and Y. Yang, "Generation and interaction of reverse and normal hairpin vortices in pipe transition," in 11th International Symposium on Turbulence and Shear Flow Phenomena, 2019.
[39]X. Wu and P. Moin, "A direct numerical simulation study on the mean velocity characteristics in turbulent pipe flow," J. Fluid Mech. **608**, 81–112 (2008).
[40]X. Wu, J. R. Baltzer, and R. J. Adrian, "Direct numerical simulation of a 30R long turbulent pipe flow at $R^+ = 685$: Large- and very large-scale motions," J. Fluid Mech. **698**, 235–281 (2012).
[41]H. Shan, B. Ma, Z. Zhang, and F. T. M. Nieuwstadt, "Direct numerical simulation of a puff and a slug in transitional cylindrical pipe flow," J. Fluid Mech. **387**, 39–60 (1999).
[42]P. Hall and N. J. Horseman, "The linear inviscid secondary instability of longitudinal vortex structures in boundary layers," J. Fluid Mech. **232**, 357–375 (1991).
[43]X. Yu and J. T. C. Liu, "The secondary instability in Görtler flow," Phys. Fluids **3**, 1845–1847 (1991).
[44]D. S. Park and P. Huerre, "Primary and secondary instabilities of the asymptotic suction boundary layer on a curved plate," J. Fluid Mech. **283**, 249–272 (1995).
[45]W. Liu and J. A. Domaradzki, "Direct numerical simulation of transition to turbulence in Görtler flow," J. Fluid Mech. **246**, 267–299 (1993).
[46]M. Asi, M. Minagawa, and M. Nishioka, "The instability and breakdown of a near-wall low-speed streak," J. Fluid Mech. **455**, 289–314 (2002).
[47]L. Brandt and H. C. de Lange, "Streak interactions and breakdown in boundary layer flows," Phys. Fluids **20**, 024107 (2008).
[48]O. Desjardins, G. Blanquart, G. Balarac, and H. Pitsch, "High order conservative finite difference scheme for variable density low Mach number turbulent flows," J. Comput. Phys. **227**, 7125–7159 (2008).
[49]Y. Yang and D. I. Pullin, "Evolution of vortex-surface fields in viscous Taylor–Green and Kida–Pelz flows," J. Fluid Mech. **685**, 146–164 (2011).
[50]Y. Zhao, Y. Yang, and S. Chen, "Evolution of material surfaces in the temporal transition in channel flow," J. Fluid Mech. **793**, 840–876 (2016).
[51]C. B. Lee and J. Z. Wu, "Transition in wall-bounded flows," Appl. Mech. Rev. **61**, 030802 (2008).
[52]M. T. Landahl, "A note on an algebraic instability of inviscid parallel shear flow," J. Fluid Mech. **98**, 243–251 (1980).
[53]P. Andersson, M. Berggren, and D. S. Henningson, "Optimal disturbances and bypass transition in boundary layers," Phys. Fluids **11**, 134–150 (1999).
[54]P. Luchini, "Reynolds-number-independent instability of the boundary layer over a flat surface: Optimal perturbations," J. Fluid Mech. **404**, 289–309 (2000).
[55]A. Tumin and E. Reshotko, "Spatial theory of optimal disturbances in boundary layers," Phys. Fluids **13**, 2097–2104 (2001).
[56]M. Shimizu and S. Kida, "A driving mechanism of a turbulent puff in pipe flow," Fluid Dyn. Res. **41**, 045501 (2009).
[57]X. Wu, R. G. Jacobs, J. C. R. Hunt, and P. A. Durbin, "Simulation of boundary layer transition induced by periodically passing wakes," J. Fluid Mech. **398**, 109–153 (1999).
[58]R. G. Jacobs and P. A. Durbin, "Simulation of bypass transition," J. Fluid Mech. **428**, 185–212 (2001).
[59]F. Waleffe, "On a self-sustaining process in shear flows," Phys. Fluids **9**, 883–900 (1997).
[60]B. Hof, C. W. H. van Doorne, J. Westerweel, F. T. M. Nieuwstadt, H. Faisst, B. Eckhardt, H. Wedin, R. R. Kerswell, and F. Waleffe, "Experimental observation of nonlinear traveling waves in turbulent pipe flow," Science **305**, 1594–1598 (2004).

[61]H. Wedin and R. R. Kerswell, "Exact coherent structures in pipe flow: Travelling wave solutions," J. Fluid Mech. **508**, 333–371 (2004).
[62]G. Kawahara, M. Uhlmann, and L. Van Veen, "The significance of simple invariant solutions in turbulent flows," Annu. Rev. Fluid Mech. **44**, 203–225 (2012).
[63]M. Chantry, A. P. Willis, and R. R. Kerswell, "Genesis of streamwise-localized solutions from globally periodic traveling waves in pipe flow," Phys. Rev. Lett. **112**, 164501 (2014).
[64]P. He and Y. Yang, "Construction of initial vortex-surface fields and Clebsch potentials for flows with high-symmetry using first integrals," Phys. Fluids **28**, 037101 (2016).